An Efficient Full-Vectorial Finite-Element Modal Analysis of Dielectric Waveguides Incorporating Inhomogeneous Elements Across Dielectric Discontinuities

Day-Uei Li and Hung-chun Chang, *Senior Member, IEEE*

***Abstract*—A new vectorial finite-element method (FEM) free of spurious modes is proposed for analyzing optical waveguides with sharp corners in the cross section. The method is formulated in terms of the transverse field components H_x and H_y or E_x and E_y, and it explicitly shows the relationships between the semivectorial and the full-vectorial wave equations. In this method, we introduce the distribution concept and an inhomogeneous element to describe the field across the dielectric interface, and the error in the numerical solution caused by the dielectric discontinuity is reduced. We show how the width of such inhomogeneous elements and the number of nodes would affect the numerical result and its convergent rate using the dielectric-loaded rectangular waveguide, the channel waveguide, and the rib waveguide as analysis examples. For the dielectric-loaded rectangular waveguide, we compare our results with the exact solutions. For the rib waveguide, we compare our results with previously published data based on other methods. Also, field convergence near the corners is discussed.**

***Index Terms*—Dielectric waveguides, finite-element method, optical waveguide theory, rectangular waveguides, rib waveguides, waveguide corner singularities.**

I. Introduction

DIELECTRIC waveguides have been fundamental structures in optoelectronic, microwave, and millimeter-wave devices. With the rapid advance of semiconductor technology, these waveguide structures can be easily integrated onto a single substrate. Various complicated waveguide structures are continuously proposed, such as directional couplers, polarizers, nonlinear optical switches, optical sensors, etc. The design of these waveguide components and the analysis of their propagation characteristics, such as birefringence and dispersion, demand highly accurate numerical methods. To meet this need, many forms of the vectorial finite-element method (VFEM) have been developed [1]–[15]. It is well known that the longitudinal E_z-H_z formulation contains mathematical singularities [1], [2]. In early years *Konrad* [3] proposed a vectorial finite-element formulation in terms of all three components of the magnetic field $\vec{H}$, which can accurately analyze the propagation characteristics of a waveguide with an arbitrary cross section. The most serious difficulty in applying the FEM to three-dimensional (3-D) inhomogeneous dielectric waveguides is the appearance of spurious solutions [4], [5]. These unphysical solutions do not satisfy the divergence-free relation $\nabla \cdot \vec{H} = 0$. To solve the spurious solution problem, there have been several methods proposed over the past 20 years [6]–[12]. The penalty function method [6]–[9] used to solve this problem can eliminate the spurious modes. At the same time, however, it causes the accuracy of solutions to be precariously dependent on the magnitude of the penalty coefficient. Some authors [10]–[12] proposed formulations in terms of transverse magnetic or electric fields by explicitly or implicitly enforcing the continuity of the tangential components of the transverse fields at the interfaces. Because most finite-element formulations utilize C^0 continuous elements to describe the fields, the added constraints would alter the optimum condition [16]. Another serious problem is that the fields near the corners could not be easily described, and the formulation is too sensitive to the type of element that we choose. A completely different way of avoiding spurious solutions using *edge elements* has also been proposed, and more generalized *tangential elements* have been developed [13]–[15]. In this formulation, usually two components of the field are expressed in terms of the edge elements and the third component is described by the node-based elements. However, in the formulations of [13] and [15], the sparsity of the matrices is lost.

In this paper, we derive in detail a highly efficient node-based full-vectorial finite-element formulation based on the transverse fields by adding inhomogeneous elements and applying the distribution concept, which are used to analyze dielectric waveguides with step dielectric discontinuities in the transverse plane. We study, by adjusting the size of the added inhomogeneous elements and the number of nodes, to what extent the interface affects the numerical result. The characteristics of this formulation include the following.

1) The numerical efficiency can be optimized since the formulation only uses the two transverse components of the field.

Manuscript received January 20, 2000; revised July 7, 2000. This work was supported in part by the National Science Council of Taiwan, R.O.C., under Grant NSC88-2215-E002-014 and Grant NSC89-2215-E002-032.

D.-U. Li is with the Department of Electrical Engineering, National Taiwan University, Taipei, Taiwan 106-17, R.O.C.

H.-C. Chang is with the Department of Electrical Engineering, Graduate Institute of Electro-Optical Engineering, and Graduate Institute of Communication Engineering, National Taiwan University, Taipei, Taiwan 106-17, R.O.C.

Publisher Item Identifier S 0018-9197(00)09764-5.

0018–9197/00$10.00 © 2000 IEEE

Authorized licensed use limited to: National Taiwan University. Downloaded on February 4, 2009 at 02:02 from IEEE Xplore. Restrictions apply.

2) The spurious solution problem is solved since the divergence-free relation for the magnetic field, $\nabla \cdot \vec{H} = 0$, is included in the formulation.
3) The final eigenvalue problem preserves the sparsity of the matrices.
4) The permittivity of the dielectric material is always continuous across any interelement interfaces.
5) The distribution of the abrupt dielectric interfaces is taken into account in the added inhomogeneous elements and, thus, corner singularities and interface singularities can be dealt with.

Moreover, C^1 continuous elements can also be utilized under this formulation for faster convergence [16].

Formulation of the present method is described in Sections II and III. Numerical results are presented in Section IV. The accuracy of the proposed method is examined and compared with previous results using other methods by using the dielectric-loaded rectangular waveguide, the channel waveguide, and the rib waveguide as examples. The conclusions are in Section V.

II. Mathematical Formulation

We consider a wave with $\exp[j(\omega t - \beta z)]$ dependence propagating in the z-direction along a dielectric waveguide, where β is the propagation constant. Maxwell's curl equations for the wave are

$$\nabla \times \vec{E} = -j\omega\mu_0 \vec{H} \tag{1}$$

$$\nabla \times \vec{H} = j\omega\epsilon_0 n^2(x, y)\vec{E} \tag{2}$$

where ϵ_0 and μ_0 are the permittivity and permeability of free space, respectively, and $n(x, y)$ is the refractive-index distribution of the waveguide. From (1) and (2), we can derive a wave equation for the transverse magnetic field component $\vec{H}_t$

$$\frac{1}{n^2}\left(\nabla_t^2 \vec{H}_t - \beta^2 \vec{H}_t\right) + k_0^2 \vec{H}_t - \nabla_t\left(\frac{1}{n^2}\right) \times \nabla_t \times \vec{H}_t = 0 \tag{3}$$

where ∇_t is the del operator in the transverse plane and k_0 is the wavenumber in free space. Note that the relation $H_z = (\nabla_t \cdot \vec{H}_t)/j\beta$ has been included in (3) and hence the spurious modes will not be present in the solution. Similarly, we can also obtain a nonhomogeneous wave equation for the transverse electric field component $\vec{E}_t$

$$\nabla_t^2 \vec{E}_t + (k_0^2 n^2 - \beta^2)\vec{E}_t + \nabla_t\left(\frac{\nabla_t n^2 \cdot \vec{E}_t}{n^2}\right) = 0. \tag{4}$$

III. The Inhomogeneous Eight-Node Element

Fig. 1(a)–(c) shows a conventional element division scheme for a waveguide at a dielectric discontinuity corner, the calculated field $\tilde{F}$ along $y = y_h$, and its derivative $\partial\tilde{F}/\partial x$, respectively. We can see that the refractive index $n(x, y)$ is piecewise continuous within each element. Equations (3) and (4) become

$$\nabla_t^2 \vec{H}_t + k_0^2 n^2 \vec{H}_t = \beta^2 \vec{H}_t \tag{5}$$

$$\nabla_t^2 \vec{E}_t + k_0^2 n^2 \vec{E}_t = \beta^2 \vec{E}_t. \tag{6}$$

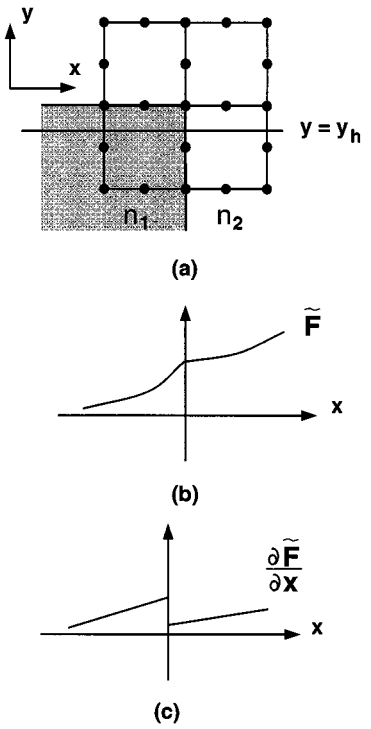

Fig. 1. (a) Conventional element division. (b) The calculated field along $y = y_h$. (c) Derivative of the calculated field with respect to x.

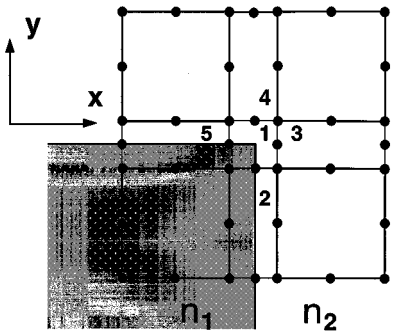

Fig. 2. Element division of the corner using inhomogeneous elements.

For C^0 elements, although the field function $\tilde{F}(x, y)$ is always continuous across the interfaces, its derivatives, for example, $\partial\tilde{F}/\partial x$, will not be continuous. Therefore, if we enforce the continuity of the field components H_z and E_z across the dielectric interfaces, the added constraints would alter the optimum condition. Especially at the corner, the continuity conditions for H_z and E_z cannot be fulfilled simultaneously. Unlike the conventional element division scheme, we divide the waveguide cross section as shown in Fig. 2. The dielectric interface is enclosed within an inhomogeneous element, and thus the dielectric constant across any interelement interface will be continuous, which implies that E_z and H_z can automatically satisfy a convergent continuity condition. If we want to ensure that H_z and E_z will be always continuous across the dielectric interfaces, we can apply the C^1 continuous elements to do the analysis. However, under the new formulation we propose, the 2-D C^0 eight-node quadratic node-based elements would be sufficient, as shown in the later numerical examples. The reason why we

Authorized licensed use limited to: National Taiwan University. Downloaded on February 4, 2009 at 02:02 from IEEE Xplore. Restrictions apply.

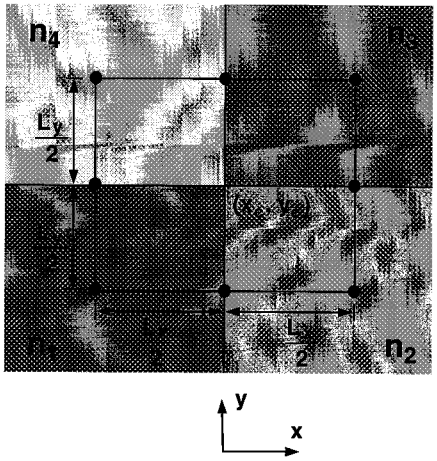

Fig. 3. An inhomogeneous element.

employ eight-node quadratic node-based elements is for their simplicity in theoretically describing the field distributions for waveguides with right-angle corners. If the corners are not of right-angle, the formulation could be modified using other coordinate transformation techniques [17].

We show in the following discussion that the dielectric interfaces will play an important role in determining the propagation characteristics. Consider an inhomogeneous element as depicted in Fig. 3, where the coordinate of the center is (x_c, y_c). We then arrange the dielectric interfaces to lie along the middle lines and use the eight-node C^0 quadratic element to describe the magnetic field components H_x and H_y. Within the element, the field components $H_{x(e)}$ and $H_{y(e)}$ could be expressed as

$$\tilde{H}_{x(e)}(x, y) = \sum_{j=1}^{8} h_{xj}\phi_{j(e)}(x, y) \tag{7}$$

$$\tilde{H}_{y(e)}(x, y) = \sum_{j=1}^{8} h_{yj}\phi_{j(e)}(x, y) \tag{8}$$

where $\phi_{j(e)}$ $(j = 1, \ldots, 8)$ represents the bases of the element. Using Galerkin's method, we multiply (3) with $\phi_{i(e)}$ $(i = 1, \ldots, 8)$, and integrate through the element $S_{(e)}$ to obtain

$$\oint_{C_{(e)}} \frac{\phi_{i(e)}}{n^2}\nabla_t H_u \cdot \hat{n}\, dl + \int_{S_{(e)}} \left[-\frac{1}{n^2}\nabla_t\phi_{i(e)} \cdot \nabla_t H_u - \phi_{i(e)}\nabla_t\left(\frac{1}{n^2}\right) \cdot \frac{\partial \vec{H}_t}{\partial u} + \left(k_0^2 - \frac{\beta^2}{n^2}\right) H_u\phi_{i(e)}\right] dx\, dy = 0 \tag{9}$$

where $u = x$ or y and $C_{(e)}$ is the boundary of the element $S_{(e)}$. The first term of (9) should be dealt with very carefully. For example, Fig. 2 shows element 1 is surrounded by elements 2, 3, 4, and 5. Since $n(x, y)$ and $\phi_{i(e)}$ are continuous, and the magnetic field and its derivatives are always continuous across the interelement boundaries by this arrangement, the contribution of the first term within the element will thus be cancelled by those of other elements. This formulation is different in the following two respects from that in [18], which claims to be able to automatically deal with various inhomogeneities in the medium. First, if $1/n^2$ is a step function, $-n^2\partial(1/n^2)/\partial u \neq (\partial(\ln n^2)/\partial u)$. Second, in [18], the continuity conditions $H(\delta) = H(-\delta)$ and $(1/\epsilon^+) \cdot \partial H(\delta)/\partial x = (1/\epsilon^-) \cdot \partial H(-\delta)/\partial x$ are enforced as two interelement boundary conditions. In fact, these constraints are only theoretically correct as $\delta \to 0$. If we really put these constraints in the numerical implementation, the results will converge to wrong values. In numerical implementation, the true constraints are $H(\delta) \to H(0)$ and $H(-\delta) \to H(0)$, and since the value of $H(0)$ is unknown, the constraints can only be included in the formulation implicitly. That is why the formulation in [18] is not suitable to deal with the sharp edge $\Delta = (\epsilon^+ - \epsilon^-)/(\epsilon^+ + \epsilon^-) \simeq 1$.

By assembling all the element equations, we have

$$\oint_C \frac{\phi_{i(e)}}{n^2}\nabla_t H_u \cdot \hat{n}\, dl + \sum_{e=1}^{N_e} \int_{S_{(e)}} \cdot \left[-\frac{1}{n^2}\nabla_t\phi_{i(e)} \cdot \nabla_t H_u - \phi_{i(e)}\nabla_t\left(\frac{1}{n^2}\right) \cdot \frac{\partial \vec{H}_t}{\partial u} + \left(k_0^2 - \frac{\beta^2}{n^2}\right) H_u\phi_{i(e)}\right] dx\, dy = 0 \tag{10}$$

where $u = x$ or y, C is the computational boundary, and N_e is the number of elements. For $u = x$, we first calculate the third term, and the following coefficients are defined:

$$q_{xx,ij} \equiv -\int_{S_{(e)}} \frac{\partial(1/n^2)}{\partial x}\,\phi_{i(e)}\,\frac{\partial\phi_{j(e)}}{\partial x}\, dx\, dy \tag{11}$$

$$p_{yx,ij} \equiv -\int_{S_{(e)}} \frac{\partial(1/n^2)}{\partial y}\,\phi_{i(e)}\,\frac{\partial\phi_{j(e)}}{\partial x}\, dx\, dy. \tag{12}$$

In order to deal with the corner singularities or the abrupt interface singularities, we introduce the distribution concept, i.e.,

$$\frac{\partial(1/n^2)}{\partial x} = \left(\frac{1}{n^2(x_c^+, y)} - \frac{1}{n^2(x_c^-, y)}\right)\delta(x - x_c) \tag{13}$$

$$\frac{\partial(1/n^2)}{\partial y} = \left(\frac{1}{n^2(x, y_c^+)} - \frac{1}{n^2(x, y_c^-)}\right)\delta(y - y_c) \tag{14}$$

and

$$\int_u f(u)\delta(u - u_c)\, du = f(u_c) \tag{15}$$

where $\delta(\cdot)$ is the Dirac delta function. Substituting (13) into (11), (11) becomes

$$q_{xx,ij} = -\int_{y_c - L_y/2}^{y_c}\left(\frac{1}{n_2^2} - \frac{1}{n_1^2}\right)\phi_{i(e)}(x_c, y)\,\frac{\partial\phi_{j(e)}}{\partial x}\bigg|_{x=x_c} dy - \int_{y_c}^{y_c + L_y/2}\left(\frac{1}{n_3^2} - \frac{1}{n_4^2}\right)\phi_{i(e)}(x_c, y)\,\frac{\partial\phi_{j(e)}}{\partial x}\bigg|_{x=x_c} dy. \tag{16}$$

Authorized licensed use limited to: National Taiwan University. Downloaded on February 4, 2009 at 02:02 from IEEE Xplore. Restrictions apply.

By assuming that $\xi = 2(x - x_c)/L_x$ and $\eta = 2(y - y_c)/L_y$, where L_x and L_y are the width and height of the element, respectively, (16) can be written as

$$q_{xx,ij} = -\frac{L_y}{L_x}\left[\left(\frac{1}{n_2^2} - \frac{1}{n_1^2}\right)\int_{-1}^{0} + \left(\frac{1}{n_3^2} - \frac{1}{n_4^2}\right)\int_{0}^{1}\right] \cdot \phi_{i(e)}(\xi = 0, \eta)\left.\frac{\partial \phi_{j(e)}}{\partial \xi}\right|_{\xi=0} d\eta. \quad (17)$$

Similarly, we can derive the expression for $p_{yx,ij}$ as

$$p_{yx,ij} = -\left[\left(\frac{1}{n_4^2} - \frac{1}{n_1^2}\right)\int_{-1}^{0} + \left(\frac{1}{n_3^2} - \frac{1}{n_2^2}\right)\int_{0}^{1}\right] \cdot \phi_{i(e)}(\xi, \eta = 0)\left.\frac{\partial \phi_{j(e)}}{\partial \xi}\right|_{\eta=0} d\xi. \quad (18)$$

The coefficient $q_{xx,ij}$ exists only when $n_1 \neq n_2$ or $n_3 \neq n_4$; that is, the dielectric discontinuity in the x direction mainly contributes to $q_{xx,ij}$. From (17), we observe that $q_{xx,ij}$ will be very large when L_x becomes small, implying that the weighting of the element containing the dielectric interface along the y direction can be very large and should not be neglected. We therefore predict that the effect on the effective index caused by the dielectric discontinuities will be very significant. Similarly, the coefficient $p_{yx,ij} \neq 0$ when $n_1 \neq n_4$ or $n_2 \neq n_3$. In the semivectorial formulation, $p_{yx,ij}$ is assumed to be zero; it can be negligible only when the waveguide is weakly guiding and the operating frequency is far away from the cutoff frequency.

We rewrite the second integral of (9) for $u = x$ as the following matrix equation:

$$([K]_e + [Q_{xx}]_e)\{h_x\}_e + [P_{yx}]_e\{h_y\}_e = \beta^2[M]_e\{h_x\}_e \quad (19)$$

where

$$[K]_{e,ij} = -\int_{S_{(e)}}\left[\frac{1}{n^2}\nabla_t\phi_{i(e)} \cdot \nabla_t\phi_{j(e)} + k_0^2\phi_{i(e)}\phi_{j(e)}\right]dx\,dy \quad (20)$$

$$[M]_{e,ij} = \int_{S_{(e)}}\frac{1}{n^2}\,\phi_{i(e)}\phi_{j(e)}\,dx\,dy \quad (21)$$

$$[Q_{xx}]_{e,ij} = q_{xx,ij} \quad (22)$$

$$[P_{yx}]_{e,ij} = p_{yx,ij} \quad (23)$$

and $\{h_x\}_e$ and $\{h_y\}_e$ are vectors composed of the x and y components, respectively, of the magnetic fields at the nodal points within the element. Similarly, for $u = y$ in (9), we can obtain

$$[P_{xy}]_e\{h_x\}_e + ([K]_e + [Q_{yy}]_e)\{h_y\}_e = \beta^2[M]_e\{h_y\}_e \quad (24)$$

where

$$[Q_{yy}]_{e,ij} = -\frac{L_x}{L_y}\left[\left(\frac{1}{n_4^2} - \frac{1}{n_1^2}\right)\int_{-1}^{0} + \left(\frac{1}{n_3^2} - \frac{1}{n_2^2}\right)\int_{0}^{1}\right] \cdot \phi_{i(e)}(\xi, \eta = 0)\left.\frac{\partial \phi_{j(e)}}{\partial \eta}\right|_{\eta=0} d\xi \quad (25)$$

$$p_{xy,ij} = -\left[\left(\frac{1}{n_2^2} - \frac{1}{n_1^2}\right)\int_{-1}^{0} + \left(\frac{1}{n_3^2} - \frac{1}{n_4^2}\right)\int_{0}^{1}\right] \cdot \phi_{i(e)}(\xi = 0, \eta)\left.\frac{\partial \phi_{j(e)}}{\partial \eta}\right|_{\xi=0} d\eta. \quad (26)$$

By assembling all the element equations, we obtain

$$\begin{bmatrix} K + Q_{xx} & P_{yx} \\ P_{xy} & K + Q_{yy} \end{bmatrix}_{2N\times 2N}\begin{bmatrix} h_x \\ h_y \end{bmatrix} = \beta^2\begin{bmatrix} M & 0 \\ 0 & M \end{bmatrix}_{2N\times 2N}\begin{bmatrix} h_x \\ h_y \end{bmatrix} \quad (27)$$

where N is the number of nodes. For the first term of (10), the computational boundary C may be a perfect electric conductor (PEC), a Dirichlet boundary, a Neumann boundary, or an infinite element boundary. After adding the contribution of the computational boundary condition, (27) can be rewritten as

$$\begin{bmatrix} K' + Q'_{xx} & P'_{yx} \\ P'_{xy} & K'' + Q''_{yy} \end{bmatrix}_{2N\times 2N}\begin{bmatrix} h_x \\ h_y \end{bmatrix} = \beta^2\begin{bmatrix} M' & 0 \\ 0 & M'' \end{bmatrix}_{2N\times 2N}\begin{bmatrix} h_x \\ h_y \end{bmatrix}. \quad (28)$$

For the semivectorial FEM formulation, $P'_{xy} = P'_{yx} = 0$, and (28) becomes

$$\left[K'^{(\prime\prime)} + Q'^{(\prime\prime)}_{uu}\right]_{N\times N}[h_u] = \beta^2\left[M'^{(\prime\prime)}\right]_{N\times N}[h_u] \quad (29)$$

where $u = x$ or y, corresponding to different polarized modes, and the prime (double prime) corresponds to $u = x(y)$. We can also derive the electric field formulation from (4) and follow the same procedure as proposed above for the magnetic field to obtain a linear equation similar to (10)

$$\oint_C \phi_{i(e)}\nabla_t E_u \cdot \hat{n}\,dl + \sum_{e=1}^{N_e}\int_{S_{(e)}} \cdot\left[-\nabla_t\phi_{i(e)} \cdot \nabla_t E_u - \frac{1}{n^2}\frac{\partial \phi_{i(e)}}{\partial u}\nabla_t n^2 \cdot \vec{E}_t + \left(k_0^2 n^2 - \beta^2\right)E_u\phi_{i(e)}\right]dx\,dy = 0. \quad (30)$$

Although there would be field singularities at the waveguide corners, it will be shown in the next section that (30) is sufficiently accurate to calculate effective indexes and field distributions.

IV. Numerical Results

In order to check the effectiveness of the full-vectorial FEM with eight-node inhomogeneous elements, we present in this section some numerical examples, including dielectric-loaded metallic rectangular waveguides, channel waveguides, and rib waveguides.

A. Dielectric-Loaded Metallic Rectangular Waveguide

Fig. 4(a) shows the cross section of a half-filled dielectric waveguide. For the fundamental LSE_{10} mode in this waveguide, the field component $H_y = 0$; hence, the field can be

Authorized licensed use limited to: National Taiwan University. Downloaded on February 4, 2009 at 02:02 from IEEE Xplore. Restrictions apply.

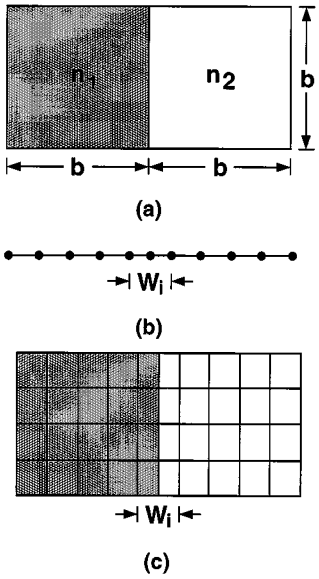

Fig. 4. Dielectric-loaded metallic rectangular waveguide. (a) Waveguide structure and (b) element division.

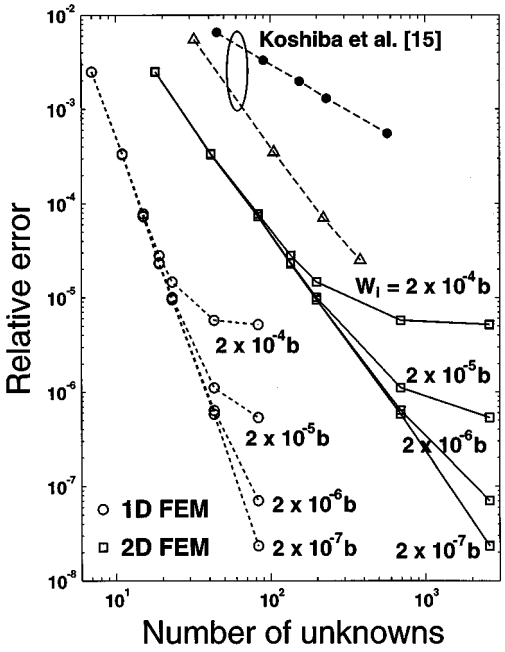

Fig. 5. Convergence of solutions using different FEMs for the fundamental LSE_{10} mode in a dielectric-loaded metallic waveguide.

approximated by one-dimensional (1-D) quadratic elements. Fig. 4(b) shows the 1-D element division scheme. To check the accuracy of our two-dimensional (2-D) full-vectorial formulation, we also use square 2-D eight-node quadratic elements with $L_x = L_y$ combined with the added inhomogeneous elements to approximate the field. Fig. 4(c) shows the 2-D element division scheme, where W_i is the width of the inhomogeneous element. The refractive indexes of the loaded dielectric and the vacuum are $n_1 = 1.5$ and $n_2 = 1.0$, respectively, and $k_0 b = 3.0$. Fig. 5 shows the relative error of the computed propagation constant β for the LSE_{10} mode using different formulations (1-D and 2-D FEMs) with different W_is ranging from $2{\cdot}10^{-7}b$ to $2{\cdot}10^{-4}b$. As

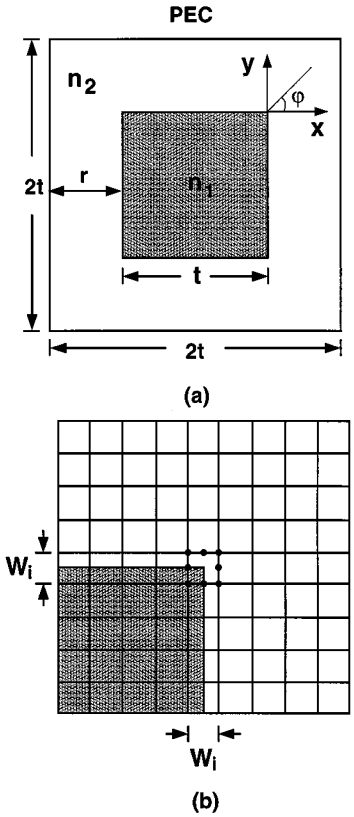

Fig. 6. Cross section of a square channel waveguide. (a) Waveguide structure. (b) Element division.

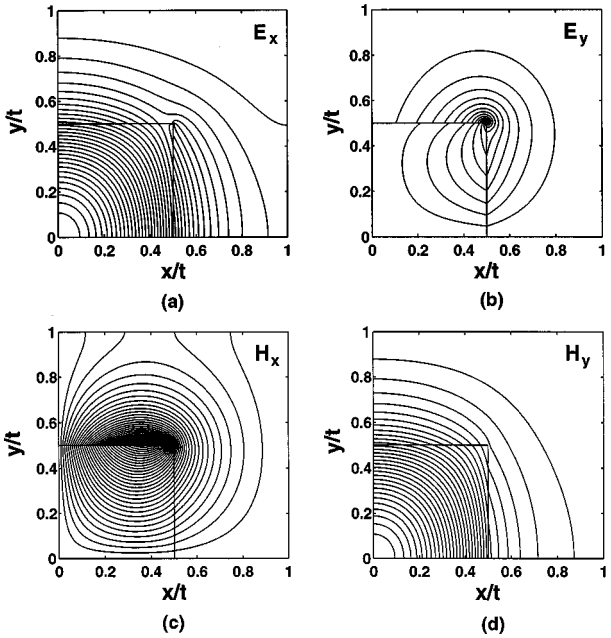

Fig. 7. Contours of the magnetic field distributions for the fundamental mode of the square channel waveguide. (a) E_x. (b) E_y. (c) H_x. (d) H_y.

in [15], the relative error is defined as $(\beta_{\mathrm{exact}} - \beta_{\mathrm{FEM}})/\beta_{\mathrm{exact}}$, where β_{exact} and β_{FEM} are the exact and the calculated values, respectively. The exact effective index for the LSE_{10} mode considered is $n_{\mathrm{eff}} = \beta_{\mathrm{exact}}/k_0 = 1.27575555$. For a mesh of 83×41 with $W_i = 2 \cdot 10^{-7}b$, the calculated effective index

Authorized licensed use limited to: National Taiwan University. Downloaded on February 4, 2009 at 02:02 from IEEE Xplore. Restrictions apply.

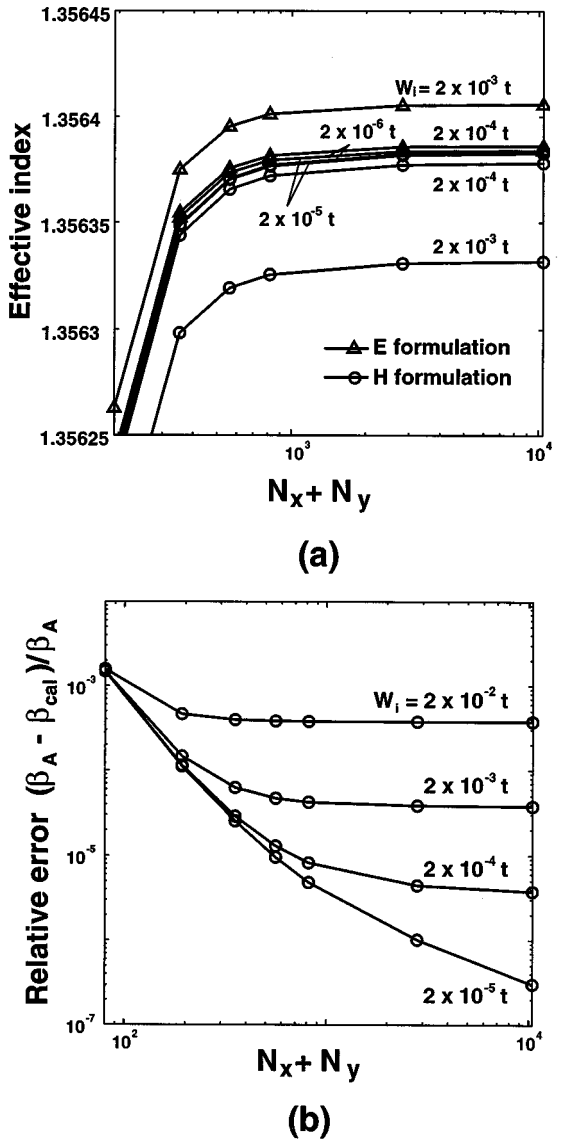

Fig. 8. (a) Effective index for the fundamental mode of the channel waveguide obtained using our H and E formulations with different W_is and (b) examination of convergence of the FEM solutions for the H formulation.

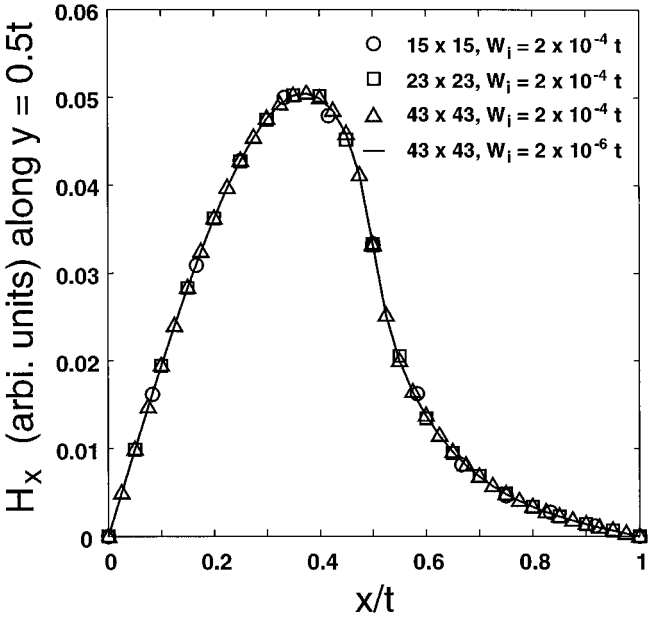

Fig. 9. Minor magnetic field profiles (H_x) along $y = 0.5t$ near the corner. Different curve represents numerical results obtained by using different division grids and different W_is.

is $n_{\text{eff}} = 1.27575552$. Compared with the exact value, the difference is on the order of 10^{-8}. In Fig. 5, we also compare our results with those obtained by Koshiba *et al.* [15]. Koshiba *et al.* employed edge elements, while we utilize nodal elements to approximate the real fields and eliminate the spurious modes. It is seen in the results of [15] that the convergence rate of the formulation with high-order mixed-interpolation-type elements (triangle data points) is much faster than that with lower order elements (black circle data points). In our calculation, as the width of the added inhomogeneous element W_i decreases and the number of the mesh points increases, the calculated results are seen to converge to the exact solution. Our formulations can give more accurate results. The computational efficiency can also be compared with edge element formulations [14] and [15]. For our formulation, the matrices storage is about $30N$, with N being the number of total unknowns, which is easily obtained by checking the number of adjacent nodes of any given node. For the method using mixed elements proposed in [15] and the formulation in [14], the matrices storage is about $60N$. For the method in [15], the formulation contains inverse matrices and the sparsity of the matrices is lost, so the matrices storage is $K \cdot N^d$, where $1 < d < 2$ and K is a constant. We can see that if the number of total unknowns is very large, the matrices storage of [15] will increase significantly.

B. Channel Waveguides

Fig. 6(a) shows the cross section of a square channel waveguide with width t and the refractive indexes of the waveguide and the vacuum being $n_1 = 1.5$ and $n_2 = 1.0$, respectively. For calculation simplicity, let us assume that there is a PEC surrounding the waveguide and $t = 2r$. By making use of structure symmetry, the computational window is designed as shown in Fig. 6(b). For the normalized frequency $V = k_0 t\sqrt{n_1^2 - n_2^2}/\pi = 2.0$, the contours of the computed field components E_x, E_y, H_x, and H_y for the fundamental mode are shown in Fig. 7(a), (b), (c), and (d), respectively. Fig. 8(a) shows the effective index as a function of the total unknowns $N_x + N_y$ for different W_is and for different formulations. $N_x(=N_y)$ is the number of nodes. Seven division grids—(7×7), (11×11), (15×15), (19×19), (23×23), (43×43), and (83×83)—were considered in the numerical computations, and the total unknowns are 80, 192, 352, 560, 816, 2816, and 10 416, respectively. We can see that as W_i decreases, the computed results converge closer to the value 1.35638307 for the H formulation and to the value 1.35638381 for the E formulation, respectively, which are the calculated effective indexes using 83×83 grid (the number of unknowns $= 2 \times (83 \times 83 - 41 \times 41) = 10\,416$) with the inhomogeneous element width $W_i = 2 \cdot 10^{-6}t$. The difference in the effective index for the H and the E formulations is about 7.4×10^{-7}. Fig. 8(b) shows the relative error of the propagation constant

Authorized licensed use limited to: National Taiwan University. Downloaded on February 4, 2009 at 02:02 from IEEE Xplore. Restrictions apply.

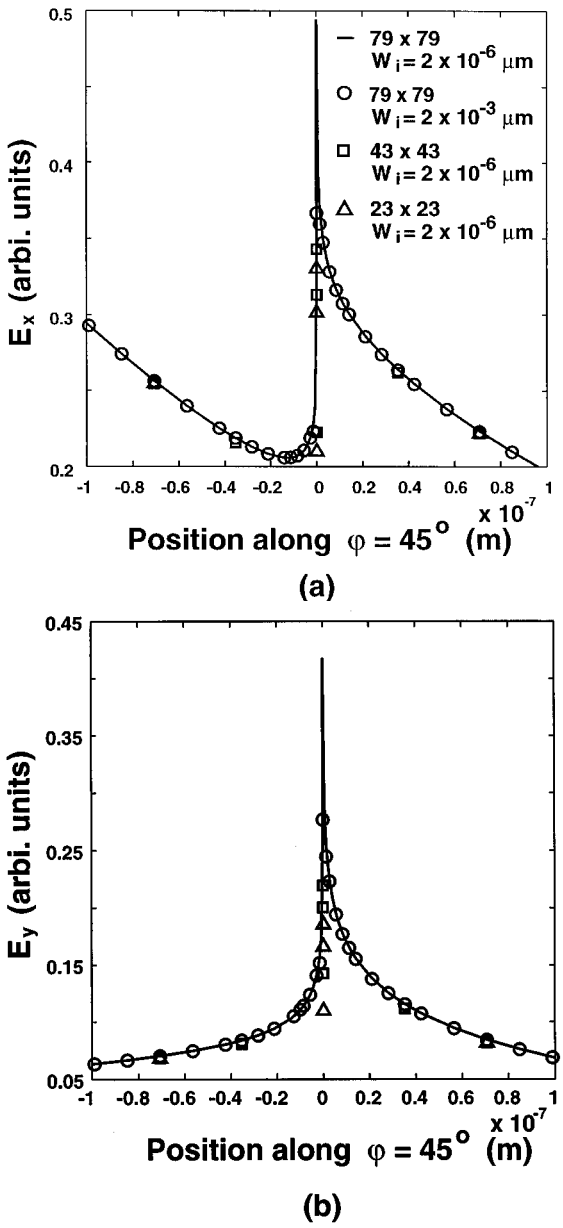

Fig. 10. Electric field profiles along the diagonal of the waveguide near a corner obtained from using different division grids and different W_is. (a) E_x. (b) E_y.

for the fundamental mode for different W_is and for the H formulation. The relative error is defined as $(\beta_A - \beta_{\text{cal}})/\beta_A$, where $\beta_A = 1.35638307k_0$ and β_{cal} is the calculated propagation constant. The convergent behavior is seen to be similar to that of Fig. 5.

Fig. 9 shows the minor field (H_x) along $y = 0.5t$ near the corner. Different curves represent numerical results obtained by using different divisions and different W_is. The field converges as the number of grid points increases. We observe that the width W_i does not significantly affect the field profile although it does affect the effective index, and that the field profile is mainly decided by the number of the grid points. From Figs. 8 and 9, although the fields have already converged with larger W_i, the effective index still varies. We observe that in this case the magnetic field singularity does not exist, so the effects caused by the corner on the effective index and the field convergence are quite small.

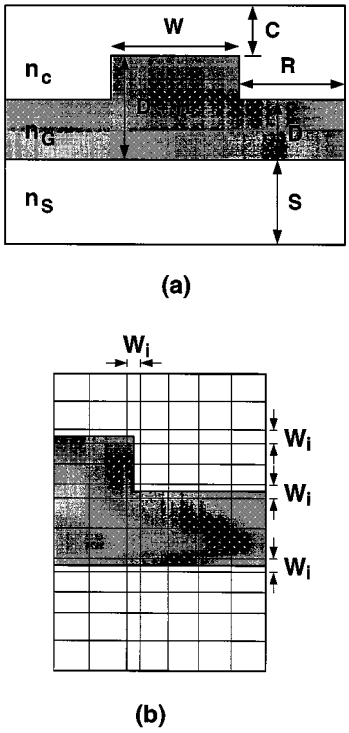

Fig. 11. (a) Cross section of a rib waveguide. (b) Element division.

In order to check the field convergence of the electric fields, we consider another square channel waveguide proposed in [19]—a square waveguide in the free space having a 1-μm width and a core refractive index $n_1 = 1.5$ operating at wavelength $\lambda = 1.5$ μm. We performed the calculation with different division grids and different W_is using the electric field formulation. Fig. 10(a) shows the major field component E_x along the diagonal of the waveguide near a corner, i.e., along $\psi = 45°$ in Fig. 6(a), where four different curves represent results obtained using different division grids (79×79, 43×43, and 23×23) and $W_i = 2 \cdot 10^{-3}$ μm or $2 \cdot 10^{-6}$ μm. The data points correspond to the positions of the grid points, and the corner is at the origin. Fig. 10(b) shows the corresponding minor field component E_y. We observe that as the grid spacing is reduced with W_i fixed at $2 \cdot 10^{-6}$ μm, the peak field value increases, while the field away from the corner has converged to some fixed value, demonstrating the divergence nature of the singularity. In the two calculations using the same division grid (79×79) but different widths of the inhomogeneous element, we find that the electric field component profiles are coincident everywhere with each other except near the corner. As W_i is reduced, the peak field value increases, showing that W_i plays an important role in the present formulation. By comparing our results with those shown in [20, Fig. 5], it can be seen that our field values at positions away from the corner converge much faster with respect to the grid spacing.

C. Semiconductor Rib Waveguides

Fig. 11(a) shows the cross section of a typical rib waveguide structure. Fig. 11(b) sketches the element division scheme when utilizing our formulation, where symmetry conditions are used.

Authorized licensed use limited to: National Taiwan University. Downloaded on February 4, 2009 at 02:02 from IEEE Xplore. Restrictions apply.

TABLE I

EFFECTIVE INDEX FOR THE RIB WAVEGUIDE, SHOWN IN FIG. 11, FOR DIFFERENT Ds COMPUTED BY DIFFERENT AUTHORS. COLUMN 1 (RAHMAN AND DAVIES [21]): VECTOR FINITE-ELEMENT METHOD. COLUMN 2 (HADLEY AND SMITH [22]): ITERATIVE FINITE-DIFFERENCE METHOD. COLUMN 3 (STERN [23]): SEMIVECTORIAL FINITE-DIFFERENCE METHOD. COLUMN 4 (ABID *et al.* [11]): VECTOR TRANSVERSE MAGNETIC FIELD FINITE-ELEMENT METHOD. COLUMN 5 (KOSHIBA *et al.* [15]): VECTOR FINITE-ELEMENT METHOD WITH HIGH-ORDER MIXED-INTERPOLATION-TYPE ELEMENTS. COLUMNS 6 AND 7: PRESENT WORK WITH A MESH OF 19 × 33 USING THE SEMI- AND FULL-VECTORIAL FEMS WITH INHOMOGENEOUS ELEMENTS WITH $W_i = 0.002$ μm

D (μm)	VFEM	FDM	SV-FDM	TFEM	Edge-FEM	SV-FEM-I	FV-FEM-I
0.0	3.41210	3.41200	3.41188	3.40970	3.41194	3.411987	3.411991
0.1	3.41220	3.41211	3.41200	3.40971	3.41209	3.412088	3.412094
0.2	3.41235	3.41226	3.41217	3.41003	3.41224	3.412237	3.412246
0.3	3.41255	3.41247	3.41240	3.41025	3.41247	3.412439	3.412449
0.4	3.41285	3.41275	3.41271	3.41057	3.41278	3.412725	3.412737
0.5	3.41315	3.41311	3.41310	3.41097	3.41312	3.413086	3.413098
0.6	3.41365	3.41355	3.41358	3.41148	3.41358	3.413526	3.413539
0.7	3.41410	3.41408	3.41415	3.41210	3.41414	3.414058	3.414069
0.8	3.41475	3.41472	3.41484	3.41298	3.41480	3.414713	3.414721
0.9	3.41560	—	3.41568	3.41446	3.41568	3.415608	3.415611

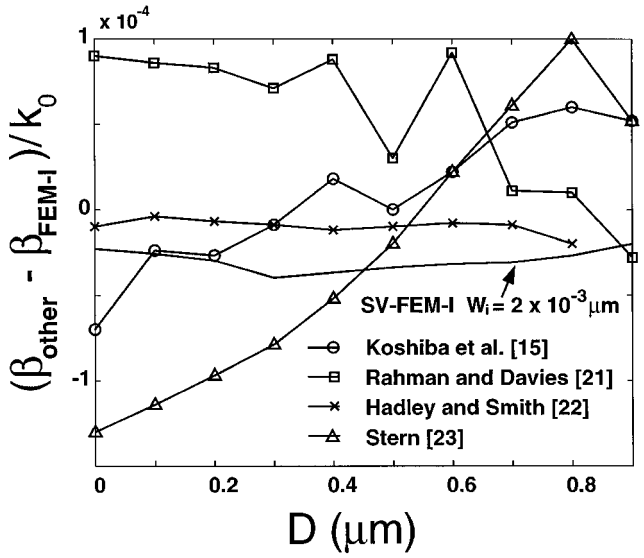

Fig. 12. Differences in the effective refractive index between other methods and the present method.

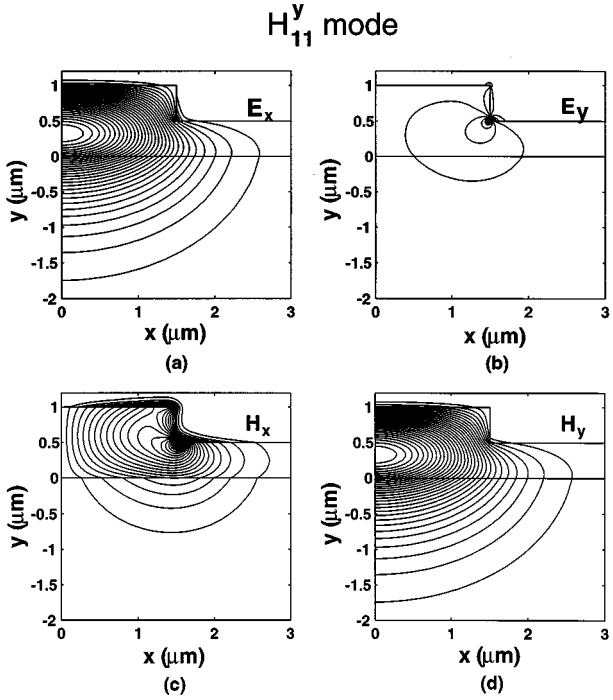

Fig. 13. Contours of the magnetic field distributions for the fundamental mode of the first rib waveguide. (a) E_x. (b) E_y. (c) H_x. (d) H_y. Only a part of the computational window is shown.

We have analyzed two well-studied semiconductor rib waveguide structures in order to compare our results with those obtained by other methods. For the first case, the operating wavelength $\lambda = 1.15$ μm, rib width $W = 3.0$ μm, and $H + D = 1.0$ μm. The outer slab depth D varies from 0 to 0.9 μm. The refractive indexes of the cover, the guiding layer, and the substrate are $n_C = 1.0$, $n_G = 3.44$, and $n_S = 3.4$, respectively. The parameters for the computational window are $R = 2.952$ μm, $C = 1.025$ μm, and $S = 5.025$ μm. We present in the last two columns of Table I the computed effective index of the lowest order H_{11}^y mode obtained by our semivectorial (SV) and full-vectorial (FV) FEMs with inhomogeneous elements (FEM-I) and with $W_i = 2 \cdot 10^{-3}$ μm. Calculations were performed using the H formulation under a mesh of 19×33 with infinite elements being used. The number of elements is $9 \times 16 = 144$, and the number of nodes is $(19 \times 33 - 9 \times 16) = 483$. Table I also provides values obtained by previous authors using different methods: the VFEM with Aitken extrapolation [21], the iterative finite-difference method (IFDM) [22], the semivectorial FDM (SV-FDM) [23], the transverse field VFEM with continuity of E_z and H_z imposed (TFEM) [11], and the VFEM with high-order mixed-interpolation-type elements (Edge-FEM) [15].

We have also used $W_i = 2 \cdot 10^{-4}$ μm and $W_i = 2 \cdot 10^{-5}$ μm and a finer grid mesh 33×53 to analyze the same waveguide. The effective indexes for different D's are shown in Table II, and the process of convergence in the calculated results is observed as the value of W_i is reduced and finer grid mesh is used. In fact, a calculation with $W_i = 2 \cdot 10^{-6}$ μm and a grid

Authorized licensed use limited to: National Taiwan University. Downloaded on February 4, 2009 at 02:02 from IEEE Xplore. Restrictions apply.

TABLE II
EFFECTIVE INDEX FOR THE RIB WAVEGUIDES, SHOWN IN FIG. 11, WITH DIFFERENT Ds OBTAINED USING THE FULL-VECTORIAL FINITE-ELEMENT FORMULATIONS WITH INHOMOGENEOUS ELEMENTS WITH DIFFERENT W_is AND MESHES

D (μm)	Grid $= 19 \times 33$ $W_i = 2 \times 10^{-4}$ μm	19×33 2×10^{-5}	33×53 2×10^{-4}	33×53 2×10^{-5}	45×53 (H) 2×10^{-5}	45×53 (E) 2×10^{-5}
0.0	3.412003	3.412004	3.412009	3.412010	3.412011	3.412011
0.1	3.412105	3.412107	3.412113	3.412114	3.412115	3.412115
0.2	3.412257	3.412258	3.412265	3.412267	3.412268	3.412268
0.3	3.412460	3.412461	3.412478	3.412479	3.412481	3.412481
0.4	3.412749	3.412750	3.412761	3.412762	3.412764	3.412764
0.5	3.413110	3.413111	3.413119	3.413120	3.413122	3.413122
0.6	3.413551	3.413552	3.413557	3.413558	3.413561	3.413561
0.7	3.414080	3.414082	3.414088	3.414089	3.414091	3.414092
0.8	3.414733	3.414734	3.414739	3.414740	3.414742	3.414742
0.9	3.415622	3.415623	3.415627	3.415628	3.415631	3.415631

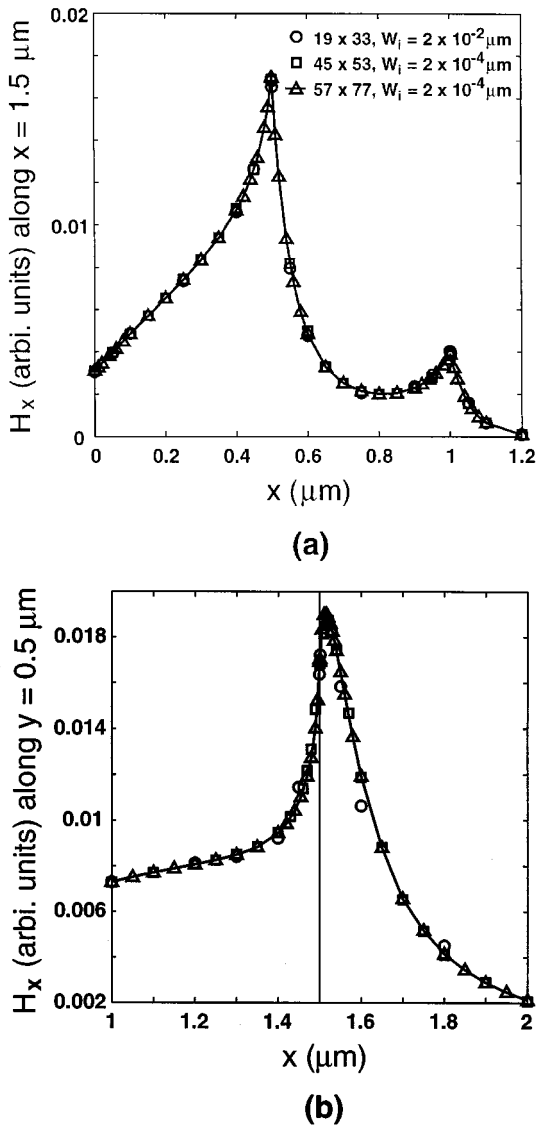

Fig. 14. Minor magnetic field profiles (H_x) along (a) $x = 1.5$ μm and (b) $y = 0.5$ μm, with different division grids and different W_i.

mesh 63×81 has also been performed, and further change in the effective index appears to be smaller than 1×10^{-6}. Fig. 12 examines the differences between the results obtained by other methods and the present method. The difference is calculated as $(\beta_{\text{other}} - \beta_{\text{FEM-I}})/k_0$, where β_{other} is the propagation constant obtained by other methods and $\beta_{\text{FEM-I}}$ is that obtained by the present full-vectorial formulation with grid mesh 33×53 and $W_i = 2 \cdot 10^{-5}$ μm. We observe that the results given by Hadley and Smith [22] using the FDM is uniformly closest to ours. We also show in this figure the difference between the result obtained by the semivectorial FEM-I with grid mesh 19×33 and $W_i = 2 \cdot 10^{-3}$ μm and the above full-vectorial result. It is clear that, in this case, we can obtain an accurate result by the semivectorial FEM-I. Fig. 13(a)–(d) shows the field contours of the field components E_x, E_y, H_x, and H_y, respectively, for $D = 0.5$ μm. Although the contours of the fields are shown, we have to check the field convergence around the waveguide corners. Fig. 14(a) and (b) shows the minor field profiles (H_x) along $x = 1.5$ μm and $y = 0.5$ μm, respectively. From Fig. 14(a), it seems that the field has converged for the rough division 19×33, while Fig. 14(b) shows that the field has not yet converged. The other division grids 45×53 and 57×77 are designed that the grid spacings near the waveguide corners are small. The effective indexes for the division grid 45×53 are shown in the last two columns of Table II for the H and the E formulations, respectively. The effective indexes obtained by the H formulation coincide well with those obtained by the E formulation. From the discussion above, we conclude that, to generally obtain the accurate effective index, we first use some rough division grid with larger W_i to locate the possible singularities. We then add some dense grid points near the field singularities to obain convergent fields, and finally reduce the width W_i to obtain the accurate effective indexes.

The second case is another rib waveguide with the rib width $W = 2.0$ μm, the outer slab thickness $D = 0.2$ μm, and $D + H = 1.3$ μm. The refractive indexes of the cover, the guiding layer, and the substrate are $n_C = 1.0$, $n_G = 3.44$, and $n_S = 3.34$, respectively. The operating wavelength is $\lambda = 1.55$ μm. The parameters for the computational window are $R = 3.0$ μm, $C = 1.7$ μm, and $S = 3.0$ μm. We used a mesh of 35×49 (the number of nodes $= 35 \times 49 - 17 \times 24 = 1307$) to calculate the propagation constant. As in the case discussed above, infinite elements were used. The effective indexes and normalized propagation constants for the H_{11}^y and

Authorized licensed use limited to: National Taiwan University. Downloaded on February 4, 2009 at 02:02 from IEEE Xplore. Restrictions apply.

TABLE III
COMPARISON OF THE EFFECTIVE INDEX n_{eff} AND THE NORMALIZED PROPAGATION CONSTANT b AT $\lambda = 1.55$ μm OBTAINED BY THE PRESENT METHOD AND OTHER METHODS

i	Method	Number of Nodes	H_{11}^y		H_{11}^x	
			n_{eff}	b	n_{eff}	b
1	VM [24]	—	3.388408	0.4804	3.387657	0.4729
2	SIM [25]	—	3.38874	0.4837	3.38788	0.4751
3	SV-BPM [26]	—	3.388711	0.4834	3.387924	0.4756
4	MMM [27]	—	3.388690	0.48322	—	—
5	SFDM [28]	1280×1280	3.388658	0.4829	3.387868	0.4750
6	FDM [29]	508×394	3.388687	0.48319	—	—
7	FEM-I (H), $W_i = 2 \times 10^{-3}$ μm	$35 \times 49 - 17 \times 24$	3.388655	0.48286	3.387829	0.47461
8	FEM-I (H), $W_i = 2 \times 10^{-4}$ μm	$35 \times 49 - 17 \times 24$	3.388684	0.48316	3.387857	0.47489
9	FEM-I (H), $W_i = 2 \times 10^{-5}$ μm	$35 \times 49 - 17 \times 24$	3.388687	0.48319	3.387859	0.47491
10	FEM-I (H), $W_i = 2 \times 10^{-6}$ μm	$35 \times 49 - 17 \times 24$	3.388687	0.48319	3.387859	0.47491
11	FEM-I (E), $W_i = 2 \times 10^{-6}$ μm	$35 \times 49 - 17 \times 24$	3.388687	0.48319	3.387859	0.47491

H_{11}^x modes using the variational method (VM) [24], the spectral index method (SIM) [25], the semivectorial beam propagation method (SV-BPM) [26], the mode-matching method (MMM) [27], the semivectorial FDM (SFDM) [28], the FDM [29], and the present method with different width W_is are summarized in Table III, where the normalized propagation constant b is defined as $(n_{\text{eff}}^2 - n_S^2)/(n_G^2 - n_S^2)$. From Table III, we can see in the last few rows that the computed results converge as we reduce the width W_i from $2 \cdot 10^{-3}$ μm to $2 \cdot 10^{-6}$ μm. Compared with those obtained by the semivectorial FDM or the full-vectorial FDM, the dimensions of the matrices in (28) are much smaller; therefore, (28) can be easily solved using personal computers.

V. CONCLUSION

A highly efficient full-vectorial node-based finite-element method for the analysis of dielectric waveguides with corners in the cross section have been proposed. We have demonstrated the convergence in the calculation of the effective index. By using the transverse field formulations and applying the distribution concept to treating the dielectric discontinuity, we have successfully analyzed structures with abrupt dielectric discontinuities and corner singularities and have successfully obtained field contributions around the dielectric interfaces. Spurious modes are totally eliminated by adding the divergence-free condition $\nabla \cdot \vec{H} = 0$ into the formulation. In Section III, we have discussed the corresponding relationship between the FEM formulations for the semi- and the full-vectorial analyzses. Compared with the conventional approaches, such as the finite-difference method, the number of nodes needed in our method is greatly reduced. The accuracy of our algorithm has been examined through several numerical examples by comparing our results with either the exact solution or the results obtained by other methods. The comparison with the edge-element method has also been made. The accuracy and efficiency of the present method are better than the edge-element method. It is shown in Section IV that, for accurately determining the propagation constant, we first locate the field singularities and then modify the formulation by adding denser grid points around the singularities to obtain the convergent fields. Lastly, we adjust the width W_i to obtain a convergent effective index. This approach can be used to analyze waveguides with inhomogeneous and/or anisotropic media and is suitable for analyzing dielectric waveguides with multilayer structure, such as multiple-quantum-well waveguides. We conclude that this method is highly efficient and accurate.

REFERENCES

[1] Z. J. Csendes and P. Silvester, "Numerical solution of dielectric loaded waveguides: I—Finite-element analysis," *IEEE Trans. Microwave Theory Tech.*, vol. MTT-18, pp. 1124–1131, 1970.

[2] P. Daly, "Hybrid-mode analysis of microstrip by finite-element methods," *IEEE Trans. Microwave Theory Tech.*, vol. MTT-19, pp. 19–25, 1971.

[3] A. Konrad, "High-order triangular finite elements for electromagnetic waves in anisotropic media," *IEEE Trans. Microwave Tech.*, vol. MTT-25, pp. 353–360, 1977.

[4] J. B. Davies, F. A. Fernandez, and G. Y. Philippou, "Finite element analysis of all modes in cavities with circular symmetry," *IEEE Trans. Microwave Theory Tech.*, vol. MTT-30, pp. 1975–1980, 1982.

[5] B. M. A. Rahman and J. B. Davies, "Finite-element analysis of optical and microwave waveguide problems," *IEEE Trans. Microwave Theory Tech.*, vol. MTT-32, pp. 20–28, 1984.

[6] M. Koshiba, K. Hayata, and M. Suzuki, "Vectorial finite-element formulation without spurious modes for dielectric waveguides," *Electron. Lett.*, vol. 20, pp. 409–410, 1984.

[7] B. M. A. Rahman and J. B. Davies, "Penalty function improvement of waveguide solution by finite elements," *IEEE Trans. Microwave Theory Tech.*, vol. MTT-32, pp. 922–928, 1984.

[8] ——, "Finite-element solution of integrated optical waveguides," *J. Lightwave Technol.*, vol. LT-2, pp. 682–688, 1984.

[9] M. Koshiba, K. Hayata, and M. Suzuki, "Improved finite-element formulation in terms of magnetic field vector for dielectric waveguides," *IEEE Trans. Microwave Theory Tech.*, vol. MTT-33, pp. 227–233, 1985.

[10] N. Mabaya, P. E. Lagasse, and P. Vandenbulcke, "Finite element analysis of optical waveguides," *IEEE Trans. Microwave Theory Tech.*, vol. MTT-29, pp. 600–605, 1981.

[11] Z. E. Abid, K. L. Johnson, and A. Gopinath, "Analysis of dielectric guides by vector transverse magnetic field finite elements," *J. Lightwave Technol.*, vol. 11, pp. 1545–1549, 1993.

[12] W. C. Chew and M. A. Nasir, "A variational analysis of anisotropic, inhomogeneous dielectric waveguides," *IEEE Trans. Microwave Theory Tech.*, vol. 37, pp. 681–688, 1989.

[13] M. Koshiba and K. Inoue, "Simple and efficient finite-element analysis of microwave and optical waveguides," *IEEE Trans. Microwave Theory Tech.*, vol. 40, pp. 371–377, 1992.

[14] J. F. Lee, D. K. Sun, and Z. J. Cendes, "Tangential vector finite element for electromagnetic field computation," *IEEE Trans. Magn.*, vol. 27, pp. 4032–4035, 1991.

[15] M. Koshiba, S. Maruyama, and K. Hirayama, "A vector finite element method with the high-order mixed-interpolation-type triangular elements for optical waveguiding problems," *J. Lightwave Technol.*, vol. 12, pp. 495–502, 1994.

[16] D. S. Burnett, *Finite Element Analysis—From Concepts to Applications*, 2nd ed. Reading, MA: Addison-Wesley, 1987.

Authorized licensed use limited to: National Taiwan University. Downloaded on February 4, 2009 at 02:02 from IEEE Xplore. Restrictions apply.

[17] I. Ergatoudis, B. M. Irons, and O. C. Zienkiewicz, "Curved, isoparametric, quadrilateral elements for finte element analysis," *Int. J. Solids Structures*, vol. 4, pp. 31–42, 1968.
[18] J. Katz, "Novel solution of 2-D waveguides using the finite element method," *Appl. Opt.*, vol. 21, pp. 2747–2750, 1982.
[19] A. S. Sudbo, "Why are accurate computations of mode fields in rectangular dielectric waveguide difficult?," *J. Lightwave Technol.*, vol. 10, pp. 418–419, 1992.
[20] W. W. Lui, C.-L. Xu, W.-P. Huang, K. Yokoyama, and S. Seki, "Full-vectorial mode analysis with considerations of field singularities at corners of optical waveguides," *J. Lightwave Technol.*, vol. 17, pp. 1509–1513, 1999.
[21] B. M. A. Rahman and J. B. Davies, "Vector-H finite-element solution of GaAs/GaAlAs rib waveguides," *Proc. Inst. Elec. Eng.*, vol. 132, pp. 349–353, 1985.
[22] G. R. Hadley and R. E. Smith, "Full-vector waveguide modeling using an iterative finite-difference method with transparent boundary conditions," *J. Lightwave Technol.*, vol. 13, pp. 465–469, 1995.
[23] M. S. Stern, "Semivectorial polarized finite difference method for optical waveguides with arbitrary index profiles," *Proc. Inst. Elec. Eng.*, pt. J, vol. 135, no. 1, pp. 56–63, 1988.
[24] W. P. Huang and H. A. Haus, "A simple variational approach to optical rib waveguides," *J. Lightwave Technol.*, vol. 9, pp. 56–61, 1991.
[25] M. S. Stern, P. C. Kendall, and P. W. A. McIlroy, "Analysis of the spectral index method for vector modes of rib waveguides," *Proc. Inst. Elec. Eng.*, pt. J, vol. 137, pp. 21–26, 1990.
[26] P. L. Liu and B. J. Li, "Semi-vectorial beam propagation method for analyzing polarized modes of rib waveguides," *IEEE J. Quantum Electron.*, vol. 28, pp. 778–782, 1992.
[27] T. Rozzi, G. Gerri, M. N. Husain, and L. Zappelli, "Variational analysis of the dielectric rib waveguide using the concept of 'transition function' and including edge singularities," *IEEE Trans. Microwave Theory Tech.*, vol. 39, pp. 247–256, 1991.
[28] H. Noro and T. Nakayama, "A new approach to scalar and semivector mode analysis of optical waveguides," *J. Lightwave Technol.*, vol. 14, pp. 1546–1556, 1996.
[29] P. Lusse, P. Stuwe, J. Schule, and H. G. Unger, "Analysis of vectorial mode fields in optical waveguides by a new finite difference method," *J. Lightwave Technol.*, vol. 12, pp. 487–493, 1994.

Day-Uei Li was born in Chiayi, Taiwan, on May 6, 1970. He received the B.S. degree from the Department of Electrical Engineering, National Taiwan University, Taipei, Taiwan, in 1992. He is currently working toward the Ph.D. degree in the same department.

His current research interests include finite element methods and the development of numerical methods for modeling optical waveguides and waveguide devices.

Hung-chun Chang (S'78–M'83–SM'00) was born in Taipei, Taiwan, Republic of China, on February 8, 1954. He received the B.S. degree from National Taiwan University, Taipei, R.O.C., in 1976, and the M.S. and Ph.D. degrees from Stanford University, Stanford, CA, in 1980 and 1983, respectively, all in electrical engineering.

From 1978 to 1984, he was with the Space, Telecommunications, and Radioscience Laboratory, Stanford University. In August 1984, he joined the faculty of the Electrical Engineering Department, National Taiwan University, where he is currently a Professor. He served as Vice-Chairman of the EE Department from 1989 to 1991, and Chairman of the newly-established Graduate Institute of Electro-Optical Engineering at the same University from 1992 to 1998. His current research interests include the theory, design, and application of guided-wave structures and devices for fiber optics, integrated optics, optoelectronics, and microwave and millimeter-wave circuits.

Dr. Chang is a member of Sigma Xi, the Phi Tau Phi Scholastic Honor Society, the Chinese Institute of Engineers, the Photonics Society of Chinese-Americans, the Optical Society of America, and China/SRS (Taipei) National Committee (a Standing Committee member during 1988–1993) and Commission H of U.S. National Committee of the International Union of Radio Science (URSI). In 1987, he was among the recipients of the Young Scientists Award at the URSI XXIInd General Assembly. In 1993, he was one of the recipients of the Distinguished Teaching Award sponsored by the Ministry of Education of the Republic of China.

Authorized licensed use limited to: National Taiwan University. Downloaded on February 4, 2009 at 02:02 from IEEE Xplore. Restrictions apply.